Journal of Magnetic Resonance 313 (2020) 106720

Contents lists available at ScienceDirect

Journal of Magnetic Resonance

journal homepage: www.elsevier.com/locate/jmr

An MRI-based switched gradient impulse response characterization method with uniform eigenmode excitation

Kulam Najmudeen Magdoom [a,*], Malisa Sarntinoranont [a,b], Thomas H. Mareci [b,c]

[a] Department of Mechanical and Aerospace Engineering, University of Florida, Gainesville, FL, United States
[b] J. Crayton Pruitt Family Department of Biomedical Engineering, University of Florida, Gainesville, FL, United States
[c] Department of Biochemistry and Molecular Biology, University of Florida, Gainesville, FL, United States

ARTICLE INFO

Article history:
Received 6 January 2020
Revised 14 March 2020
Accepted 16 March 2020
Available online 17 March 2020

Keywords:
Gradient pre-emphasis
Eddy currents
Mechanical resonance
MRI based field monitoring

ABSTRACT

Switching gradients generate eddy currents and mechanical vibrations of the gradient assembly causing errors in the gradient time integrals. This results in image distortions in k-space and inaccuracies in q-space imaging. The purpose of this work is to develop an MRI based unbiased measurement of the switched gradient impulse response function (sGIRF). A new gradient pattern, called the Tukey windowed Shifted Sine-Integral (Tw-SSI) pulse, is introduced to excite the gradient eigenmodes uniformly over a user-defined bandwidth. A 3D MRI-based method with Hadamard encoding was developed to map the spatiotemporal magnetic field generated after the excitation pulse to obtain the sGIRF for all the three gradient axes simultaneously. Compared to an energy-equivalent traditional trapezoidal pulse, the Tw-SSI pulse is able to excite the weak bandlimited cross-terms of the sGIRF by uniformly distributing the energy across eigenmodes. The developed field mapping method is sensitive enough to capture both the direct and cross-terms in the sGIRF. The various mechanical resonant modes of the gradient coils are also revealed, which were found to last longer than eddy currents in the shielded gradient coil studied. Tunable Tw-SSI pulse offers the flexibility to perform unbiased sGIRF measurements over a bandwidth of interest. Rapid MRI field mapping can be easily implemented in any MRI system. The method may be used to perform gradient pre-emphasis, to evaluate new gradient coil designs, and to characterize higher order shims.

1. Introduction

Pulsed magnetic field gradient (PFG) measurements are effected by residual magnetic fields, persisting long after the pulse, due to eddy currents generated in surrounding conducting structures [1], and mechanical vibration of the gradient assembly [2,3]. Errors in gradient time integrals cause image distortions in diffusion MRI [4] and introduce artifacts in velocity measurements using phase contrast MRI [5]. These errors exacerbate in the measurement of very low diffusivity or flow velocities, which often require strong gradients. Eddy current fields are typically minimized by overdriving the gradient amplifiers through gradient pre-emphasis [6], while the effect of mechanical vibrations is reduced by an appropriate choice of the echo time [7] or using an oscillatory pre-emphasis unit [8].

Efficient gradient pre-emphasis depends on accurately determining the gradient system switching characteristics described by the switched gradient impulse response function (sGIRF). The term 'switched' distinguishes sGIRF from the standard gradient impulse response function (GIRF) used to characterize the gradient systems [9–11]. GIRF represents the overall transfer function of the gradient system without particular emphasis on switching characteristic, since it is quantified by deconvolving the measured response with the test gradient pulse rather than its derivative (i.e. switching characteristic). On the other hand, sGIRF is particularly sensitive to gradient switching which is the source of eddy currents and mechanical vibrations of the gradient assembly described by a superposition of discrete eigenmodes [12,13]. An ideal sGIRF measurement requires a uniform broad-band excitation of these gradient eigenmodes (both eddy current and mechanical) using a test gradient pattern followed by immediate measurement of the residual magnetic field at high spatiotemporal resolution. The sGIRF is then generalized for any arbitrary gradient pattern assuming the gradient system is linear and time invariant [14].

---

* Corresponding author at: Department of Mechanical and Aerospace Engineering, University of Florida, Gainesville, FL 32611, United States.

E-mail address: kulamnajmudeem2@mail.nih.gov (K.N. Magdoom).

https://doi.org/10.1016/j.jmr.2020.106720
1090-7807/Published by Elsevier Inc.

The frequency spectrum of the test gradient derivative provides the eigenmode excitation profile, which modulates the actual response of the system [15]. A trapezoid [16–19] is a common test gradient shape, which has a non-uniform sinc-like excitation spectrum with several nulls (i.e. Fourier transform of the derivative of a ramp function is a sinc). This also introduces a bias in the measurement for low frequency eigenmodes. In addition, the trapezoid plateau time needs to be kept much longer than the gradient eigenmode decay time constants to ensure the fields from ascending and descending ramps do not cancel each other. However, extending this time to counteract very long time constants increases the gradient temperature, which is known to affect the gradient mechanical resonance frequencies [20], and possibly introduce gradient independent field changes, e.g. concomitant heating of passive shims, confounding the measurement [21]. In addition, the trapezoidal shape does not provide easy control over the excited eigenmodes, which could span several orders in magnitude [18]. A gradient pattern capable of uniformly exciting the eigenmodes within a specified bandwidth would allow an unbiased measurement of sGIRF and be useful in designing bandwidth-optimized measurement protocols.

Owing to superior sensitivity and ease of detection, residual magnetic fields from the test gradient pulse are usually measured in the phase of the proton NMR spectrum at multiple time points after the pulse. Robertson et al. [19] measured the spatial variation in the fields by moving the sample, while Spees et al. [18] used samples with different chemical shifts arranged in a lattice. Recent techniques involve field camera measurements, which use multiple NMR probes arranged in a sphere, to sample the 4D field with high spatial and temporal resolution [9,10]. However, the hardware is complex and custom built for the system under study. MR imaging-based techniques overcome the need for customization by allowing implementation across different systems without any special hardware, however current methods lack the speed and capability to measure higher order shim fields for practical applications. Boesch et al. used a stimulated echo multi-slice imaging sequence to measure the field [22]. Bhogal et al. applied the same technique in a 3D gradient echo imaging sequence [23]. These imaging methods naturally provide a high spatial resolution but obtaining high temporal resolution comes at the cost of increasing acquisition time. Terpstra et al. improved the method developed by Boesch et al. by replacing 2D multi-slice imaging with 1D projections along three orthogonal axes to reduce the acquisition time [24]. However, this method does not allow detection of nonlinear terms, such as xy, xz, and yz, which are important for characterizing shim coils

In this study, a novel test gradient pulse pattern is developed that is capable of uniformly exciting the gradient eigenmodes within a specified frequency bandwidth of interest. In addition, a 3D gradient multi-echo imaging-based technique is introduced to rapidly map the spatiotemporal magnetic fields generated after the test gradient pulse. The multi-echo approach allows higher temporal resolution with fewer repetitions compared to currently available single echo approaches. The 3D imaging capability also enables characterization of higher order shim fields unlike the Boesch's method [24].

2. Materials and methods

2.1. Lumped model for eigenmodes

The eddy current and mechanical eigenmodes are modeled as inductance-resistance circuits [25] and spring-mass-dampers, respectively. Since the residual field obeys harmonic equations and is dominated by lower degree spherical harmonics, its spatial variation is approximated up to the first order using a trilinear equation (Equation 10.35 in [15]). Assuming the gradient system is linear and time-invariant [6,25], the intercept, $b_0(t)$, and slope, $\vec{g}(t)$, of the residual field after an uniaxial test gradient pulse, $G_a(t)$, is modeled as a convolution of the time derivative of $G_a(t)$ and impulse response functions for the static and gradient fields respectively which constitute the sGIRF (Equation 10.39 and 10.40 in [15]). Each of these impulse response functions, $h(t)$, is modeled as a sum of decaying exponentials to account for eddy current eigenmodes, and decaying sinusoids to account for the mechanical eigenmodes,

$$h(t) = \sum_{i=1}^{n} \alpha_i e^{-\frac{t}{\tau_i}} + \sum_{j=1}^{m} \beta_j \sin\left(2\pi f_j t + \phi_j\right) e^{-\frac{t}{\kappa_j}} \quad (1)$$

where α_i, τ_i are the amplitude and time constant of i^{th} eddy current eigenmode, $\beta_j, \kappa_j, f_j, \phi_j$ are the amplitude, time constant, frequency and phase, respectively, of the j^{th} mechanical eigenmode.

2.2. Eigenmode excitation

From the convolution theorem, an unbiased estimate of the sGIRF requires the spectrum of the excitation gradient pulse derivative be uniform over a specified bandwidth. In order to capture short time constants decaying after the pulse, the time between eigenmode excitation and measurement must be minimal. The following shifted *sinc* function fits the above criteria, since its spectrum is a rectangular function of width, Δf, and the excitation time is controlled using the shift factor, η,

$$\frac{dG_a}{dt} = A\text{sinc}[2\pi\Delta f(t - \eta T)] \quad (2)$$

where A is the pulse amplitude and T is the duration. The following gradient shape is a solution to the above equation, with the initial condition, $G_a(t = 0) = 0$.

$$G_a(t) = A(\text{Si}[2\pi\Delta f(t - \eta T)] + \text{Si}[2\pi\Delta f\eta T]) \quad (3)$$

where Si is the sine-integral function,

$$\text{Si}[t] = \int_0^t \text{sinc}(\text{t})dt \quad (4)$$

The gradient shape of Eq. (3) is not well behaved, since it does not go to zero at the end of the pulse. To enforce this condition, the shape is windowed with the following Tukey function [26], $W(t,\lambda)$.

$$W(t,\lambda) = \begin{cases} 1 & 0 < t \le (1-\lambda)T \\ \sin^2\left[\frac{\pi(t-T)}{2T\lambda}\right] & (1-\lambda)T < t \le T \end{cases} \quad (5)$$

where λ is the window factor controlling the relative lengths of constant and sinusoidal portion of the Tukey function. The Tukey windowed, shifted sine integral (Tw-SSI) test gradient pulse, G_{aw}, is,

$$G_{aw}(t) = G_a(t)W(t,\lambda) \quad (6)$$

Fig. 1A–C shows a plot of this function, along with its derivative and excitation spectrum. Fig. 1D shows the approximate time of excitation using the wavelet scalogram, which plots the frequency content of the gradient derivative over time and shows that the bulk of the excitation occurs at $t = \eta T$ with the selected bandwidth. For comparison, Fig. 2 shows the eigenmode excitation pattern for the traditional trapezoidal gradient of identical duration.

2.3. Field mapping

The z-component of the magnetic field generated by the test gradient pulse is determined at multiple time points using a

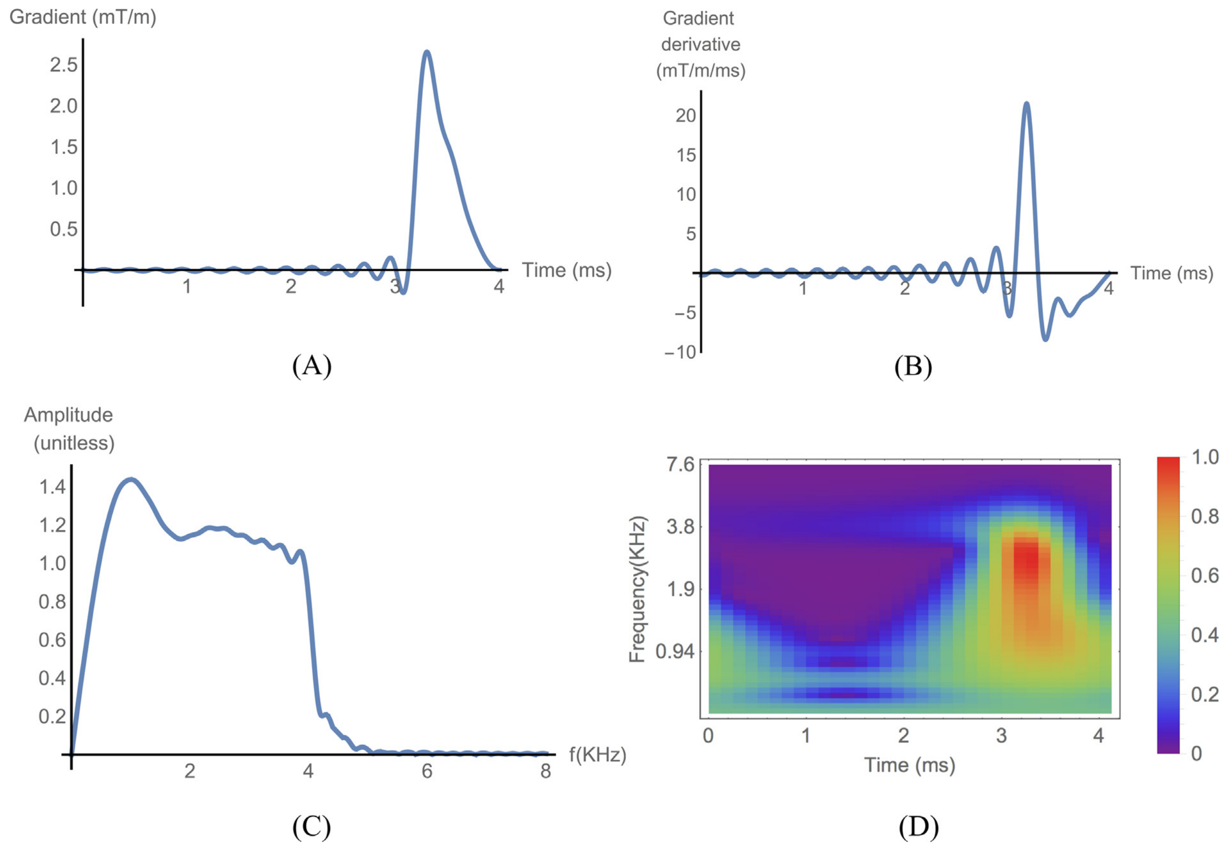

Fig. 1. Tukey windowed, shifted sine-integral (Tw-SSI) gradient pulse of 4 ms duration and 4 kHz bandwidth with the bulk of excitation occurring at 3.2 ms. (A) Gradient pattern used to drive the amplifier, (B) derivative of the gradient pattern showing the sinc excitation in time domain, (C) Fourier transform of the gradient derivative showing the bandlimited excitation spectrum in frequency domain, and (D) Wavelet transform of the gradient derivative showing the time point at which the excitation occurs (i.e. at 3.2 ms).

multi-gradient-echo imaging pulse sequence. The Tw-SSI gradient pulse followed by a variable delay, δ, is applied before the slab-selective RF pulse, as shown in Fig. 3A. Multiple echoes allow acquisition of multiple time points in a single shot thus reducing the overall acquisition time. However, this does not limit the sampling period to the echo spacing, since arbitrary temporal resolution is obtained in an interlaced fashion by incrementing δ (Fig. 3B). The response along each gradient axes is characterized by applying the Tw-SSI pulse on all the axes with gradient polarities systematically varied according to four-step Hadamard encoding (Table 24.1 in [27]). The phase, φ_b, for each gradient axis is extracted from the complex signal, S_i, at the i^{th} Hadamard step using,

$$\varphi_b^{read} = \frac{1}{4}\arg\left(\frac{S_2 \cdot S_3}{S_1 \cdot S_4}\right), \varphi_b^{phase} = \frac{1}{4}\arg\left(\frac{S_2 \cdot S_4}{S_1 \cdot S_3}\right),$$
$$\varphi_b^{slice} = \frac{1}{4}\arg\left(\frac{S_3 \cdot S_4}{S_1 \cdot S_2}\right) \tag{7}$$

The magnetic field response for each gradient axis is extracted by taking the time derivative of these phase terms,

$$B_z\left(\vec{r}, t+\delta\right) = \frac{1}{\gamma}\frac{d\varphi_b}{dt} \tag{8}$$

Phase unwrapping was performed in 3D space, if necessary, using an algorithm outlined in [28]. It was also performed in time, before the numerical derivative approximation using forward differencing, using an IDL (Harris Geospatial Solutions, Broomfield, Colorado) library function, *phunwrap*.

2.4. Gradient amplifier response measurement

Since the frequency response of the gradient-amplifier/coil limit the bandwidth of the Tw-SSI pulse, the response was measured with the amplifier connected to the gradient coil and driven with a chirp pulse using a linear frequency sweep from zero to 22.5 kHz in 20 ms at 3% maximum gradient amplitude (Fig. 4A). The gradient digital-to-analog converter (DAC) input and the amplifier output were simultaneously recorded (Picoscope Model 5444B, Pico Technology North America Inc, TX). The amplifier transfer function was calculated by taking the Fourier transform of the ratio of output and input waveforms.

2.5. MRI measurements

MRI measurements used a 330 mm inner diameter (ID) Oxford 4.7 T horizontal bore magnet and Agilent VNMRS imaging console, controlled by VnmrJ3.1A software (Agilent Technologies, Santa Clara, CA), with 115 mm ID RRI BFG-200/115-S14 gradients (Resonance Research, Billerica, MA), which has 80 mm diameter linear spherical volume with maximum gradient strength and slew rate equal to 670 mT/m and ~5600 T/m/s respectively for all three axis, driven by IECO GPA-400–750 3-axis gradient amplifiers (International Electric Co., Helsinki, Finland) and transmit-receive 88 mm ID custom quadrature birdcage RF coil. Measurements were performed after zeroing gradient pre-emphasis settings.

Measurements were performed on 0.6% hydrogel (w/v), in a 66 mm ID round bottom flask, doped with 27 mM copper sulfate pentahydrate to reduce the T_1/T_2 relaxation times. A hydrogel

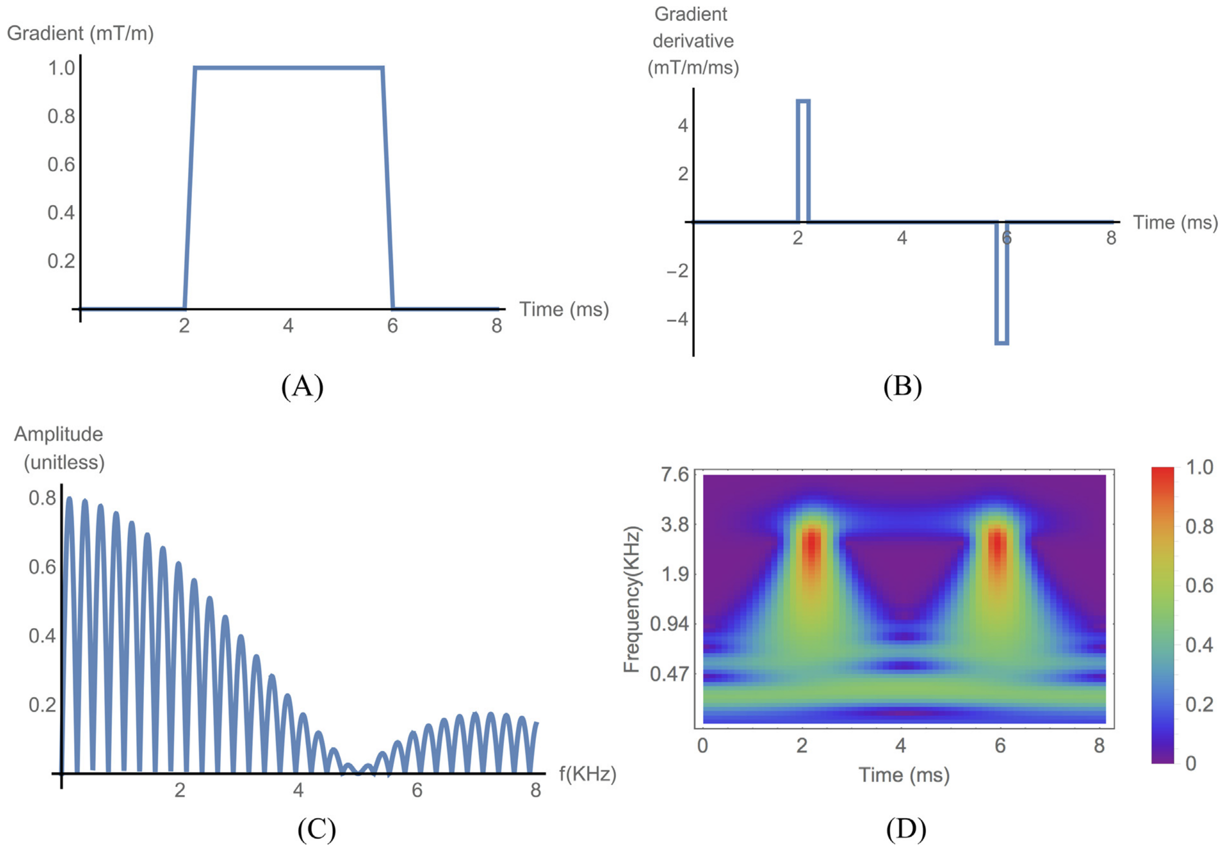

Fig. 2. Trapezoidal gradient pulse of 4 ms duration and 200 µs rise time. (A) Gradient pattern used to drive the amplifier, (B) derivative of the gradient pattern showing the bipolar impulse excitation in time domain, (C) Fourier transform of the gradient derivative showing the sinc-type excitation spectrum in frequency domain, and (D) Wavelet transform of the gradient derivative showing the time points at which the excitation occurs.

hampers fluid motion resulting from natural convection flows, which may induce velocity-dependent phase errors [29,30]. The large sample size provides greater sensitivity to slow-spatially varying magnetic field while remaining within the linearity volume of the gradient coil. Sample T_1 and T_2 were measured to choose TR such that the spin phase memory is fresh before each RF excitation. T_1 was quantified using inversion recovery spectroscopy with TR = 2500 ms and TI = 5.625, 11.25, 22.5, 45, 90 and 180 ms, and T_2 with a Carr-Purcell-Meiboom-Gill sequence using TR = 2500 ms, TE = 1 ms and 128 echoes.

The sGIRF was measured with the MRI technique shown in Fig. 3 using TR = 250 ms, TE = 0.3 ms, echo spacing = 0.5 ms and 24 echoes with a Tw-SSI gradient pulse duration of 4 ms, excitation bandwidth of 4 kHz, $\eta = 0.8$ and $\lambda = 0.25$ and peak gradient amplitudes of 480, 300, 240 mT/m on x, y and z gradients, respectively, chosen to prevent phase wrapping. For the Tw-SSI pulse, the resulting maximum gradient slew rates were approximately equal to 4000, 2500 and 2000 T/m/s on x, y and z gradients respectively. The excitation bandwidth was matched with the bandwidth of the gradient amplifier (Fig. 4) to maintain the fidelity of the Tw-SSI pulse. The window factor, λ, was chosen to reduce the truncation ripples in the frequency response. The δ delay ranged from 0.05 to 0.45 ms in steps of 0.1 ms to obtain a field sampling frequency of 10 kHz for a total duration of 12.27 ms. The field of view was 66 mm × 66 mm × 66 mm to encompass the whole spherical volume, in a matrix of 32 × 32 × 32. The total acquisition time was approximately 1.5 h for all three gradient axes combined. A short TR was chosen to reduce the acquisition time but long enough to prevent field carryover to successive TR intervals which was verified with a 500 ms TR acquisition.

The sGIRF was measured twice to ensure temporal stability of the gradient system and reproducibility of the fitted parameters. To evaluate the bandwidth property of the Tw-SSI pulse, two responses were measured with excitation bandwidth set to 1 kHz and 4 kHz. The 1 kHz excitation used a 16 ms pulse duration to maintain the time-bandwidth product. However, since the measured response also depends on the time between excitation and start of reception, the 4 kHz excitation used $\eta = 0.2$, so that this time was 3.2 ms for both the acquisitions.

The measured sGIRF for the Tw-SSI pulse was compared with a trapezoidal pulse of identical duration with the peak gradient strength adjusted such that the root-mean-square current was the same as the Tw-SSI pulse resulting in 200, 125, 100 mT/m with ramp times equal to 36, 24, 20 µs on x, y, z gradients, respectively. This prevents temperature changes in the gradient coil from altering the response [20].

2.6. Data processing

As discussed in Section 2.1, the dynamics of $b_0(t)$ and $\vec{g}(t)$, generated after the Tw-SSI gradient pulse, are calculated by fitting the time-dependent 3D field (Eq. (8)) to a trilinear equation using the Levenberg-Marquardt least squares IDL library function, MPFIT [31]. To prevent overfitting, several sub-model cases were used (e.g. b_0, $g_x x$, $b_0 + g_x x$, $g_y y$, $b_0 + g_y y$, etc.) and the model which best explained the variance in the data was chosen. The calculated $b_0(t)$ and $\vec{g}(t)$ were deconvolved with the test gradient pulse and Fourier transformed to obtain the frequency domain sGIRF. Since the excitation spectrum of the Tw-SSI pulse is approximately

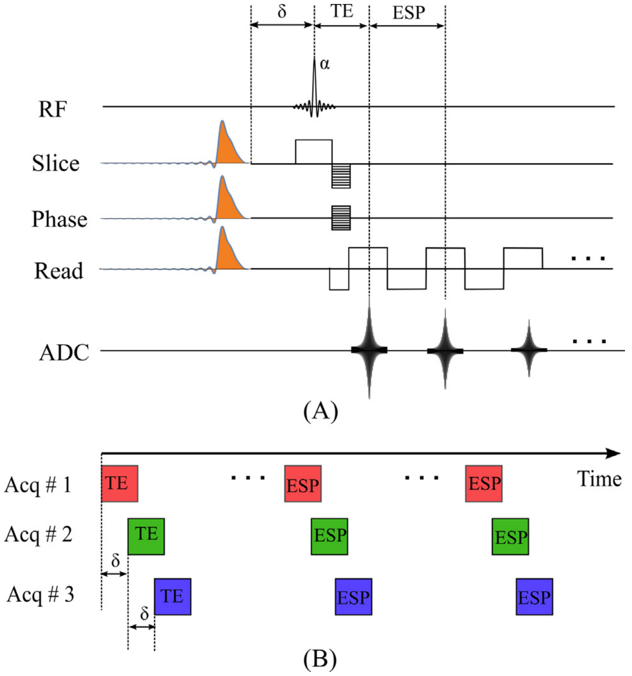

Fig. 3. MRI technique to sense the residual field from a test gradient pulse along with the temporal field sampling scheme. (A) Multi-gradient echo pulse sequence with a test gradient (i.e. Tw-SSI) before the slab-selective radiofrequency (RF) pulse for field reception. Tw-SSI gradient pulse used to excite the gradient eigenmodes is highlighted in orange. δ, TE are the delay and echo times respectively, and ESP is the echo spacing and α is the flip angle of the RF pulse. (B) Interlaced scheme showing three separate acquisitions to sample the generated field at arbitrary temporal resolution set by δ. The acquisitions are shifted by integer multiples of δ to cover the time axis as shown in the figure. (For interpretation of the references to colour in this figure legend, the reader is referred to the web version of this article.)

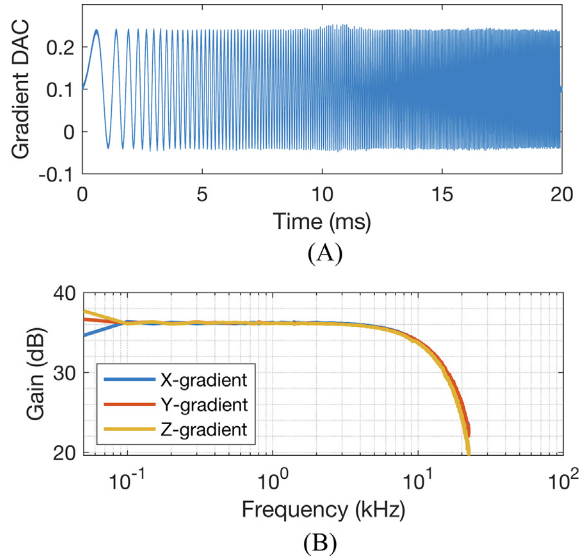

Fig. 4. Frequency response of the gradient amplifier for x-, y- and z- gradient coils. (A) Output from the gradient DAC showing the chirp gradient pulse with frequency linearly swept from 0 to 22.5 kHz in 20 ms used to drive the amplifier, and (B) Bode diagram showing amplifier gain versus frequency.

rectangular, the deconvolution step simplifies to scaling by the relative peak gradient strength on the three axes.

The unknown parameters ($\alpha, \tau, \beta, \kappa, f$ and ϕ) were found by fitting the model to the measured $b_0(t)$ and $\vec{g}(t)$ using MPFIT. The model for $b_0(t)$ and $\vec{g}(t)$ was obtained analytically by solving the convolution integrals (Equation 10.39 and 10.40 in [15]) using Eqs. (1) and (6) for impulse response function and excitation gradient pattern respectively. Since the eddy current amplitude is usually much larger than the oscillatory component, modeling is performed in two steps to improve the fit. First, the measurement was fitted to the eddy current model ($\beta = 0$), then the residual was fit to the oscillatory model ($\alpha = 0$). Parsimony was also imposed on the model fitting using the F-test [32] to prevent over-fitting, and eddy current and oscillatory amplitudes were constrained to be less than 5%. Time constants were constrained to be greater than the excitation pulse inverse bandwidth or half the echo time whichever is larger.

3. Results

The average relaxation times were $T_1 = 39 \pm 7.5$ ms and $T_2 = 31.25 \pm 5.5$ ms, so relaxation was complete for the gradient response measurement TR of 250 ms. The frequency response of the gradient amplifiers/coils is shown in Fig. 4B. A plot of the amplifier gain versus input current frequency exhibited a low-pass-filter type amplifier response beginning to decline after approximately 4 kHz.

Using the 4 kHz bandwidth Tw-SSI pulse, Fig. 5 shows the twice measured time-domain sGIRF along with the model fit (solid lines). The model fit for the measured responses was in good agreement with the data ($R^2 > 0.5$) from both the repetitions except for a few cases (e.g. y-gradient generated by pulsing the x-gradient in run 1). The fitted parameters provided in Tables 1, 2 and 3 for x-, y- and z-gradient coils respectively were also similar across the repetitions. The parameters obtained using the energy equivalent trapezoidal pulse are included in the tables for comparison. Using the Tw-SSI pulse, the field measurement technique captured the b_0 field, strong direct gradient response fields (e.g. x-gradient field produced by pulsing x-gradient) and the orders-of-magnitude weaker cross-interaction gradient response fields (e.g. y-gradient field produced by pulsing x-gradient) generated after the Tw-SSI pulse for all the three gradient axes. The R^2 value for the model fit obtained with the trapezoidal pulse clearly showed it was able to elicit only the direct gradient response, hence the cross-interaction gradient response obtained using the pulse are not discussed further.

Using the Tw-SSI pulse, the fields decayed with a single time constant of approximately 300 µs. The trapezoidal pulse resulted in direct eddy current amplitudes and time constants lower than that obtained using the Tw-SSI pulse for all the three gradient axes. The parameters characterizing the cross-interaction gradient response using Tw-SSI pulse were similar across both measurements. However, the y- and z-gradients generated by pulsing x-gradient had different time constants and amplitudes despite similar data as shown by Fig. 5C and D. The z-gradient generated by pulsing y-gradient had slightly different time constant with similar amplitudes, but opposite sign. The y-gradient generated by pulsing the z-gradient had different time constants and amplitudes despite similar data as shown in Fig. 5K.

The method also captured the weak mechanical response of the gradient coils. The mechanical resonance frequency for the direct x- and y-gradient response fields were approximately equal to 500 Hz, while the z-gradient had a frequency of 650 Hz. The amplitudes of the mechanical oscillations and signs of the frequency varied across the repetitions mainly due to the differences in fitted phase (e.g. b_0 response of x-gradient coil in Table 1) or the picked resonant mode of the gradient coil (e.g. direct gradient response of x-gradient in Table 1). Mechanical oscillations and cross-gradient response fields typically persisted for a much longer period with time constants on the order of several milliseconds. The eddy cur-

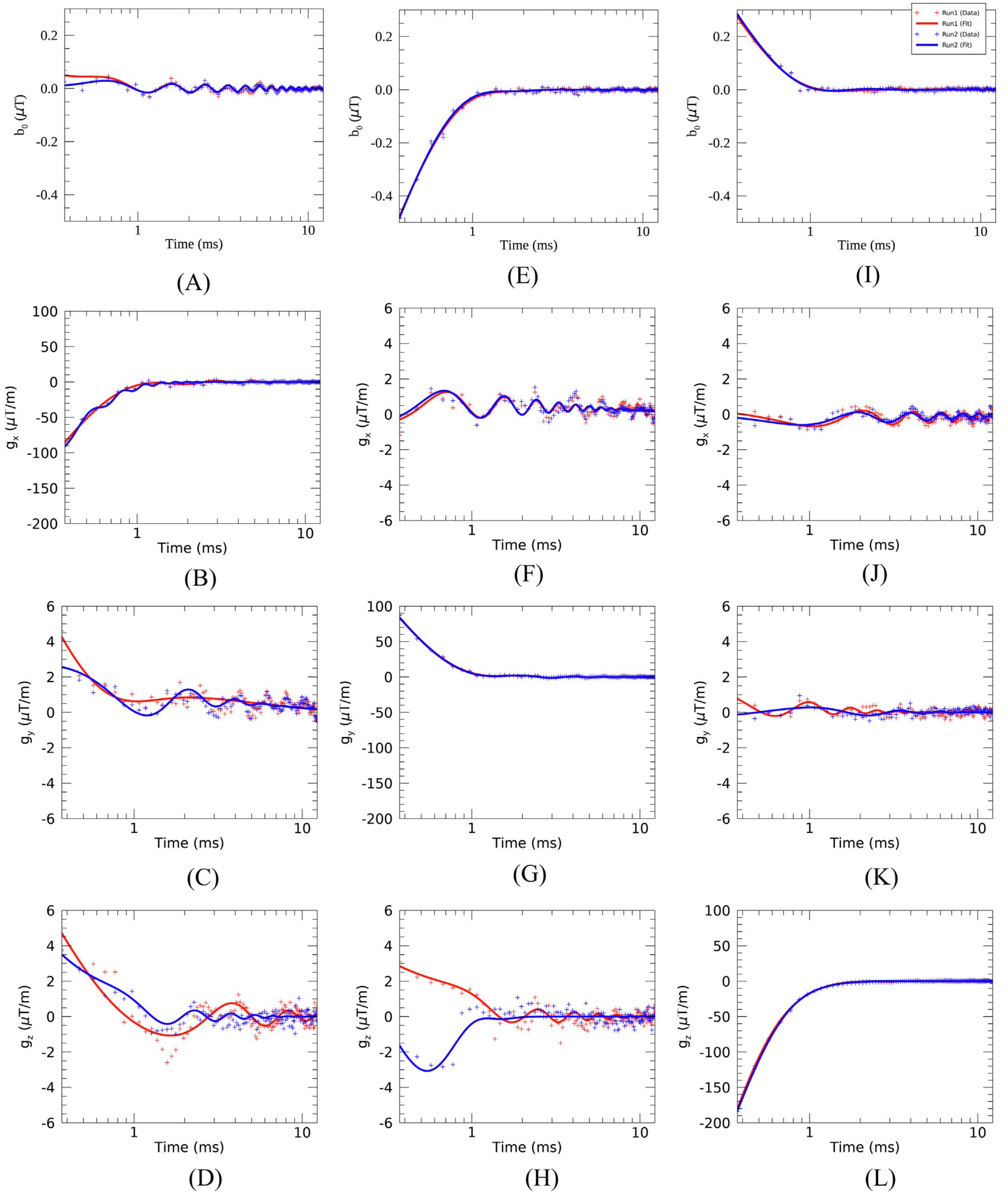

Fig. 5. Time domain gradient response (plus symbol) obtained using 4 kHz bandwidth Tw-SSI excitation repeated twice (run 1 and run 2) along with model fit (solid lines). (A–D) b_0, x, y, z gradient fields respectively generated by pulsing the x-gradient coil, (E–H) b_0, x, y, z gradient fields respectively generated by pulsing the y-gradient coil, and (I–L) b_0, x, y, z gradient fields respectively generated by pulsing the z-gradient coil.

rent amplitude of direct gradient field was orders of magnitude higher compared to mechanical oscillations.

Fourier transforming the measured time domain sGIRF shows the effect of repetition time on the measured sGIRF for TR = 250 and 500 ms (Fig. 6). In the frequency domain, exponentially decaying eddy current fields appear as Lorentzian functions centered at zero frequency (e.g. Fig. 6L), while the mechanical response appear at frequencies associated with oscillations (e.g. Fig. 6B arrows).

Table 1

Eq. (1) model fit parameters for x-gradient excitation obtained using Tw-SSI pulse with 4 kHz bandwidth for 4 ms repeated twice (run 1 and run 2) along with that obtained using an energy equivalent trapezoidal pulse rounded to three significant figures. The eddy current amplitude, α, and mechanical oscillation amplitude, β, of the gradient response field, g_i, are expressed as the percent of the applied test gradient strength, and in μT/mT/m for the b_0 response field. The time constant associated with eddy currents, τ, and mechanical oscillations, κ, along with the frequency of oscillation, f, and phase, ϕ, are also included. The goodness fit was measured using the coefficient of determination, R^2.

Distortion	Pulse shape	α	τ (ms)	β	κ (ms)	f (kHz)	ϕ (rad)	R^2
b_0 (μT/mT/m)	Tw-SSI (Run 1)	−5.00E−2	0.268	1.54E−2	5.46	−1.11	0.929	0.641
	Tw-SSI (Run 2)	−3.69E−4	0.347	1.39E−2	5.98	1.10	2.20	0.567
	Trapezoid	1.02E−3	0.948	−27.4	0.186	−0.915	−0.518	0.370
g_x (%)	Tw-SSI (Run 1)	5.00	0.270	−1.40E−5	3.23	0.496	0.275	0.981
	Tw-SSI (Run 2)	5.00	0.269	−7.57E−3	0.644	−3.43	−0.958	0.980
	Trapezoid	−0.875	0.186	−0.290	0.186	0.825	0.931	0.986
g_y (%)	Tw-SSI (Run 1)	−1.65E−5	5.79	0.178	0.324	0.0227	−0.419	0.525
	Tw-SSI (Run 2)	−1.17E−5	7.61	−1.83E−5	1.61	−0.536	1.47	0.515
	Trapezoid	1.39E−2	0.417	4.84E−4	24.5	−0.881	0.976	0.318
g_z (%)	Tw-SSI (Run 1)	−5.00	0.265	1.46E−5	5.77	−0.225	−0.849	0.664
	Tw-SSI (Run 2)	−3.25E−2	0.290	1.55E−5	2.24	−0.679	2.68	0.684
	Trapezoid	−6.77E−4	8.10	1.01E−2	0.471	0.715	−2.44	0.0982

Table 2

Eq. (1) model fit parameters for y-gradient excitation obtained using Tw-SSI pulse with 4 kHz bandwidth for 4 ms repeated twice (run 1 and run 2) along with that obtained using an energy equivalent trapezoidal pulse rounded to three significant figures. The eddy current amplitude, α, and mechanical oscillation amplitude, β, of the gradient response field, g_i, are expressed as the percent of the applied test gradient strength, and in μT/mT/m for the b_0 response field. The time constant associated with eddy currents, τ, and mechanical oscillations, κ, along with the frequency of oscillation, f, and phase, ϕ, are also included. The goodness fit was measured using the coefficient of determination, R^2.

Distortion	Pulse shape	α	τ (ms)	β	κ (ms)	f (kHz)	ϕ (rad)	R^2
b_0 (μT/mT/m)	Tw-SSI (Run 1)	5.00E−2	0.295	0.172	0.529	−0.443	−1.06	0.988
	Tw-SSI (Run 2)	5.00E−2	0.294	−0.225	0.532	0.442	1.07	0.988
	Trapezoid	1.14E−4	3.97	0.792	1.78	4.95	−1.28	0.0971
g_x (%)	Tw-SSI (Run 1)	−8.89E−6	14.7	−1.44E−4	2.21	1.17	−1.89	0.303
	Tw-SSI (Run 2)	−1.02E−5	10.1	1.34E−4	2.40	−1.15	1.47	0.382
	Trapezoid	−0.0174	0.390	4.01E−3	4.79	−4.78	0.775	0.211
g_y (%)	Tw-SSI (Run 1)	−5.00	0.272	−1.74E−5	3.02	0.494	−2.87	0.993
	Tw-SSI (Run 2)	−5.00	0.272	−3.50E−5	2.23	0.495	−2.89	0.994
	Trapezoid	0.809	0.186	−0.206	0.186	−1.73	1.43	0.963
g_z (%)	Tw-SSI (Run 1)	−2.38E−3	0.434	1.01E−5	4.00	0.632	0.603	0.685
	Tw-SSI (Run 2)	5.40E−3	0.364	−5.32E−2	0.280	−0.958	1.56	0.566
	Trapezoid	−2.33E−4	8.00	−0.172	0.186	−0.775	−1.07	0.11

Table 3

Eq. (1) model fit parameters for z-gradient excitation obtained using Tw-SSI pulse with 4 kHz bandwidth for 4 ms repeated twice (run 1 and run 2) ran twice along with that obtained using an energy equivalent trapezoidal pulse rounded to three significant figures. The eddy current amplitude, α, and mechanical oscillation amplitude, β, of the gradient response field, g_i, are expressed as the percent of the applied test gradient strength, and in μT/mT/m for the b_0 response field. The time constant associated with eddy currents, τ, and mechanical oscillations, κ, along with the frequency of oscillation, f, and phase, ϕ, are also included. The goodness fit was measured using the coefficient of determination, R^2.

Distortion	Pulse shape	α	τ (ms)	β	κ (ms)	f (kHz)	ϕ (rad)	R^2
b_0 (μT/mT/m)	Tw-SSI (Run 1)	−5.00E−2	0.287	0.411	0.512	−0.245	−0.208	0.975
	Tw-SSI (Run 2)	−5.00E−2	0.288	−0.143	0.622	0.369	−1.21	0.977
	Trapezoid	1.49E−2	0.198	−0.289	24.5	3.21	−1.42	0.263
g_x (%)	Tw-SSI (Run 1)	4.86E−6	24.5	−9.14E−7	10.1	0.489	−2.55	0.584
	Tw-SSI (Run 2)	6.07E−6	8.22	9.19E−7	7.55	0.491	0.814	0.430
	Trapezoid	−0.0329	0.186	−1.14E−3	24.5	−3.18	−1.11	0.263
g_y (%)	Tw-SSI (Run 1)	−4.53E−5	0.930	3.27E−4	1.01	−1.31	−0.505	0.309
	Tw-SSI (Run 2)	5.00	0.265	5.22E−6	2.53	−0.410	−2.00	0.143
	Trapezoid	−4.02E−2	0.186	3.38E−3	4.38	−2.95	0.325	0.164
g_z (%)	Tw-SSI (Run 1)	5.00	0.281	0.194	0.237	0.652	3.07	0.999
	Tw-SSI (Run 2)	5.00	0.282	2.48E−2	0.358	0.634	2.56	0.999
	Trapezoid	−2.25	0.186	0.0575	0.341	−1.54	0.991	0.990

Comparing different TR results, b_0 and direct gradient response fields did not show any significant differences. Plotting the response in the frequency domain also reveals several resonant modes which were not visible in the fit, likely due to the imposed model parsimony. The direct gradient field response shows x- and y-gradient coil resonances at approximately 546, 1134 and 3400 Hz (Fig. 6B and 6G), while the z-gradient did not appear to resonate. Resonant peaks in the cross-term gradient field response matched the resonance frequency of the gradient coil generating the field. For example, the x-gradient response field (Fig. 6J) produced by pulsing the z-gradient had a resonance peak at 546 Hz, corresponding to one of the resonance modes of the x-gradient coil, as shown in Fig. 6B. Also, such behavior was observed on the x-gradient field response (Fig. 6F) produced by pulsing the y-gradient, and z-gradient field response (Fig. 6D) produced by pulsing the x-gradient.

Fig. 7 shows the effect of varying the excitation bandwidth. Fig. 7B and 7G illustrate the bandlimited response, where the 1.1 kHz and 3.4 kHz resonant modes of the x- and y- gradient coils was suppressed for 1 kHz bandwidth. Since the time between excitation and reception was longer (compare Fig. 6), high-amplitude, short time-constant eddy current was suppressed, revealing a previously hidden resonance modes of the z-gradient coil approximately at 125 and 630 Hz, as shown in Fig. 7L.

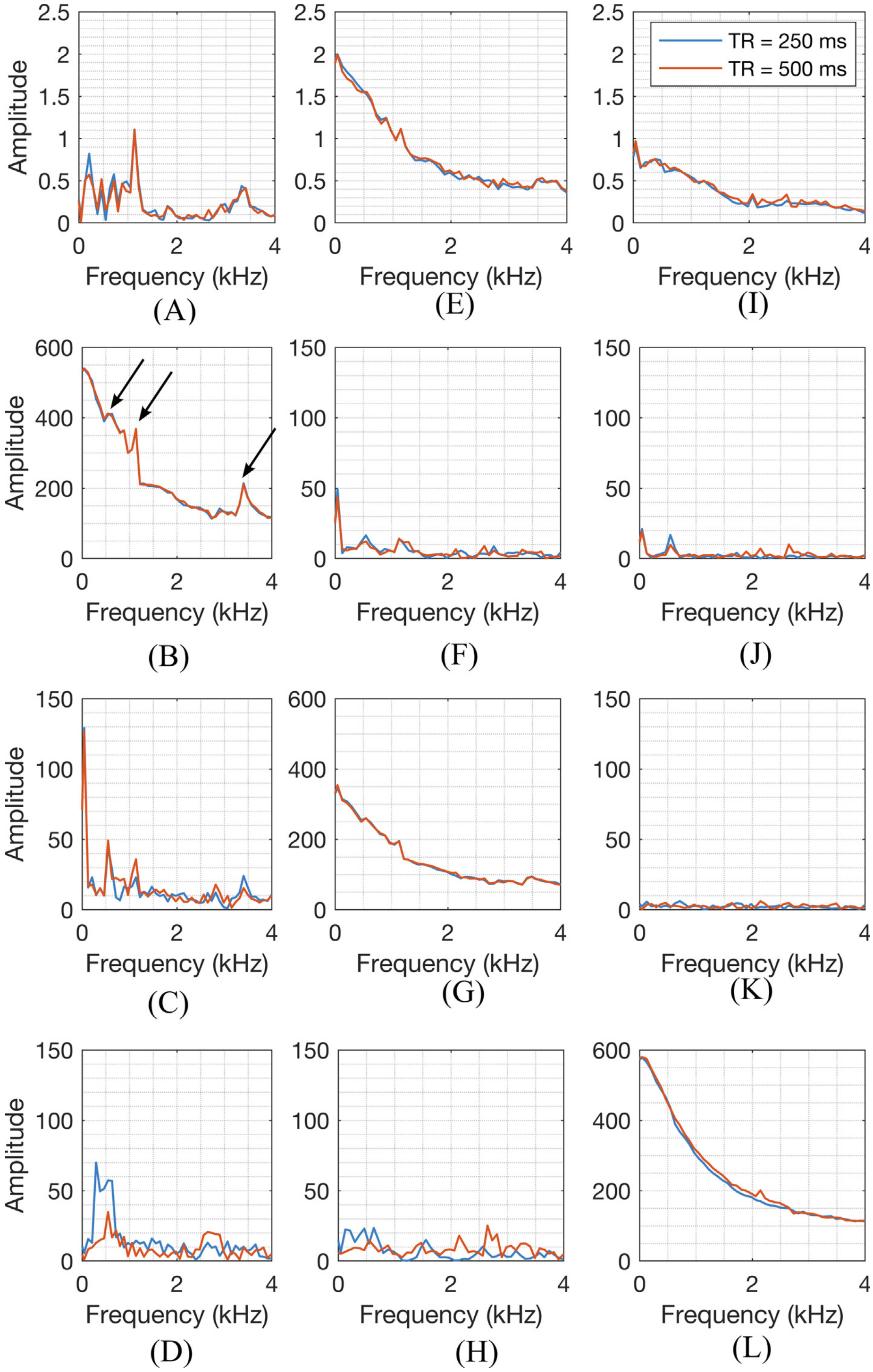

Fig. 6. Effect of varying TR on the measured filtered sGIRF shown by the Fourier spectrum for all three gradient axes. Measurement was performed using the Tw-SSI gradient pulse with 4 kHz excitation bandwidth for 4 ms with TR = 250 ms and 500 ms. (A–D) b_0, x, y, z gradient fields respectively generated by pulsing the x-gradient coil, (E–H) b_0, x, y, z gradient fields respectively generated by pulsing the y-gradient coil, and (I–L) b_0, x, y, z gradient fields respectively generated by pulsing the z-gradient coil. The mechanical resonance frequencies of the x-gradient coil are shown using arrows in B.

4. Discussion

This study developed an MRI method to rapidly excite and measure fields generated by gradient switching with potential applications to improving PFG experiments. A new gradient pulse shape, called Tw-SSI, was introduced for uniform eigenmode excitation over a bandwidth within the capabilities of a gradient system under study. Magnetic fields were rapidly sampled shortly after excitation using a multi-gradient-echo 3D MRI sequence. The method was able to characterize the eddy current and mechanical eigenmodes for all three axes simultaneously using Hadamard encoding.

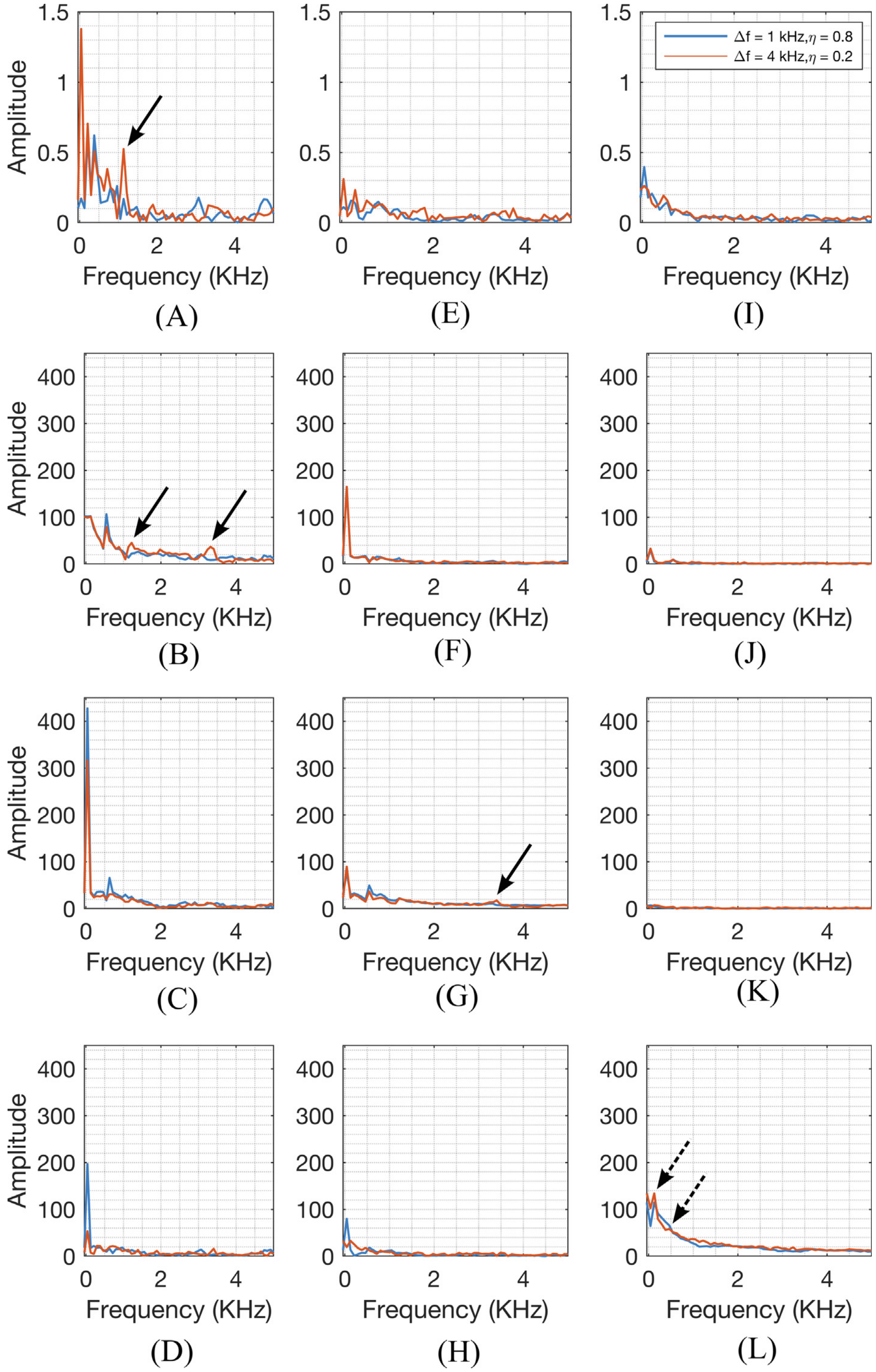

Fig. 7. Effect of varying excitation bandwidth (1 and 4 kHz) on the measured filtered sGIRF while maintaining the time-bandwidth product of the pulse. The shift parameter, η, for the 4 kHz bandwidth pulse was reduced to keep the time between field excitation and reception constant. (A–D) b_0, x, y, z gradient fields respectively generated by pulsing the x-gradient coil, (E–H) b_0, x, y, z gradient fields respectively generated by pulsing the y-gradient coil, and (I–L) b_0, x, y, z gradient fields respectively generated by pulsing the z-gradient coil. Suppression of the 1.12 and 3.40 kHz resonant mode of the x- and y-gradient coil by the 1 kHz bandwidth Tw-SSI pulse is shown by arrows in A, B and G. The resonance modes of z-gradient coil at 125 and 630 Hz are shown using dashed arrows in L.

4.1. Excitation gradient pulse

To the best of our knowledge, the importance of excitation gradient pulse has been studied previously for GIRF measurements [11,33] but not for the sGIRF. Vannesjo et al. used chirp shaped gradient pulses for measuring GIRF by spreading the pulse energy uniformly across a specified band of frequencies [11]. However, sGIRF measurement with chirp-pulse has limitations; (1) the measurement is biased towards high frequencies, since the sGIRF depends on test gradient derivative whose Fourier transform is the gradient spectrum weighted by the frequency, (2) chirp pulses excite eigenmodes sequentially (typically from low to high frequencies), which allows low-frequency eigenmodes to decay before readout.

The effect of uniform excitation energy across the eigenmodes is evident from comparing the gradient responses measured with Tw-SSI and energy equivalent trapezoidal pulses. The broadband sinc-like excitation spectrum of the trapezoidal pulse rendered the cross-terms invisible, because the pulse energy in the bandwidth containing the cross-terms was not sufficient for excitation. The results also showed the trapezoidal pulse underestimated the direct eddy current amplitudes and time constants, despite having a good fit. This is likely due to the ill-posed nature of phase unwrapping involved in the field map calculation with multiple phase jumps between voxels from overexcitation of low frequency eigenmodes.

The other advantage of the new excitation gradient pulse is the capability to tune the excitation bandwidth, which was illustrated by suppression of high frequency eigenmodes in the x- and y-gradient coils using a smaller bandwidth pulse (Fig. 7). Variable bandwidth tuning allows selective probing of eigenmodes, which typically span several orders of magnitude in strength and frequency.

4.2. Eigenmodes and Pre-emphasis

The gradient response and model parameter fitting were reproducible, except for a few cross-term cases likely due to low SNR (see Fig. 5H). Model fitting results for all the three gradient coils showed a single dominant eddy current eigenmode of very high amplitude and sub millisecond time constant. The equal small-time constant value on all three gradient axes suggests identical coupling with a small and/or less conductive structure, which implies the source might be the RF shield or a small structure intrinsic to the gradient set. Large amplitude, long-time constant eddy currents were not observed likely due to gradient shielding.

For this particular gradient system under study, longer time constant responses arise mainly from mechanical oscillations of the gradient assembly. Fourier analysis showed multiple resonance frequencies which were identical for the x- and y-gradient coils, but different from the z-gradient coil. Roozen et al. has shown that the mechanical eigenmodes excited by x- and y-gradient coils are different from that of the z-gradient coil due to the nature of the Lorentz forces acting on the coils [3]. Often the z-gradient coil is a wire structure while the x- and y-gradient coils are etched copper plate patterns, which might explain the different resonant modes observed. Observation of x-gradient resonance modes for z-gradient excitation implies that pulsing one gradient coil vibrates the other two coils in the set. This suggests that the oscillations in the cross terms could be reduced by mechanically isolating the individual gradient coils better perhaps by winding them in separate formers with gaps in between.

Model fit parameters might allow the design of pre-emphasis gradient waveforms to reduce eddy currents. Compared to other methods, this method of uniform eigenmode excitation and sensitive field detection improves the accuracy of pre-emphasis setting. However for this gradient system, pre-emphasis was not performed since the dominant eddy current amplitude was very large and the time constants too small to be corrected using the limited bandwidth of the amplifier [15]. Compensating the effects of mechanical resonance requires an oscillatory pre-emphasis unit, such as the one described in [8], not available in this system.

4.3. Field reception

MRI based gradient field reception methods have been developed in several previous studies [22–24], however the application of these methods is limited by long acquisition times compared to the state-of-the-art field camera measurements [9–11]. The MRI method in the present study uses Hadamard encoding and a multi-echo pulse sequence with adequate sampling frequency to allow the response of all the three gradient axes to be measured in a reasonable amount of time. The multiple readouts in a single TR enable higher temporal resolution with fewer repetitions of the acquisition.

The MRI based method introduced here has enough sensitivity to measure both the strong direct and weak cross magnetic fields of the gradient response. The spatial and temporal resolution of the measured field could easily be tailored for the gradient/shim system under study without need for field camera hardware. However, the field camera does provide far greater temporal resolution (56 kHz [11]) in a shorter acquisition time. However, such high sampling frequency might not be required with the limited bandwidth of typical gradient amplifier/coil systems.

4.4. Translation to whole-body MR systems

As discussed below, this methodology could be adapted to whole-body MRI systems. The strength of the Tw-SSI pulse would need to be lowered to reflect the lower gradient strength and slew rates available in the whole-body clinical gradients. For example, Tw-SSI pulse for a typical whole-body MR system with maximum gradient strength and slew rate less than 45 mT/m and 200 T/m/s respectively, would have a peak gradient amplitude of 20 mT/m for a duration of 4 ms with bandwidth equal to 4 kHz. Increasing the pulse bandwidth to 8 kHz would require a gradient strength of 10 mT/m while remaining within the slew rate limit.

The loss in sensitivity to residual magnetic fields due to lowered gradient strength is however compensated by several factors. The large size of the clinical gradient systems exacerbates the amplitude of eddy currents and mechanical vibrations making them easier to detect [34]. Multiple receiver channels available in clinical systems improves SNR which in turn improves the phase measurement sensitivity [27]. The large linear volume of whole-body MR gradients (i.e. 500–600 mm diameter compared to 80 mm used in this study) allows samples much bigger than that used in this study, which in turn increases the accuracy of the linear fit to weak magnetic fields.

The repetition time of the imaging sequence also needs to be increased to accommodate longer-time constants eddy currents in whole body systems [35]. The resulting long acquisition time could be reduced by increasing the number of echoes, and use of parallel imaging to reduce the number of phase encoding steps [36]. The signal loss resulting from more echoes is minimized by lengthening sample T_2^* with a uniform susceptibility sample and advanced shimming [37,38]. Additionally, the lower B_0 field strength of most clinical scanners helps reduce field inhomogeneity effects. For time constants much longer than the T_2^* of the sample, the field sampling time could be arbitrarily increased using multiple shots by shifting the imaging block in Fig. 3B after the last echo of the previous shot.

4.5. Limitations

The method presented here has limitations: (1) To estimate the pre-emphasis constants accurately, the field generated immediately after the pulse must be sampled, which is limited by the echo time of the sequence. The shortest achievable TE depends on the gradient amplifier bandwidth and peak gradient slew rate. (2) The efficiency of the acquisition depends on the shortest achievable echo spacing which depends on the gradient hardware and receiver switching time. (3) This imaging-based approach assumes the field generated after the test gradient pulse is small enough not to cause geometric distortions in the image. These effects are exacerbated in fast imaging with very short TE and ESP, since the magnitude of the generated field is very large immediately after the test gradient pulse. However, this could be partly overcome by adjusting the peak gradient strength of the pulse.

4.6. Future work

This method might be used to design flow or diffusion gradient shapes optimized to eliminate artifacts, and improve new gradient coil designs, e.g. by increasing the stiffness of the gradient coils to shift the mechanical resonance frequencies beyond the amplifier/coil excitation bandwidth. Given the 3D imaging capability, the pulse sequence can be used to characterize higher order shim gradient switching which is used for non-linear spatial encoding. These non-linear shim fields have been thought to reduce peripheral nerve stimulation, a factor which limits the gradient performance especially in human MRI [39,40].

Funding

This work was supported in part by the NIH/NCATS Clinical and Translational Science Award UL1 TR000064, and National High Magnetic Field Laboratory pilot study grant.

Declaration of Competing Interest

The authors declare that they have no known competing financial interests or personal relationships that could have appeared to influence the work reported in this paper.

Acknowledgements

A portion of this work was performed in the Advanced MRI/S (AMRIS) Facility at the McKnight Brain Institute of the University of Florida, which is part of the National High Magnetic Field Laboratory (NHMFL) supported by National Science Foundation Cooperative Agreement DMR-1157490, the State of Florida, and the U.S. Department of Energy. We would like to thank Dr. Alan Rath and Alex Karpovich from Agilent technologies for advice on pulse programming and hardware. We would also like to thank Dr. William W. Brey from NHMFL for advice on gradient pulse shapes, and Dr. Huadong Zeng and Malathy Elumalai from the AMRIS facility for assisting with experiments.

References

[1] W.S. Price, Pulsed-field gradient nuclear magnetic resonance as a tool for studying translational diffusion: Part II. Experimental aspects, Concepts Magn. Reson. 10 (1998) 197–237, https://doi.org/10.1002/(SICI)1099-0534(1998)10:4<197:: AID-CMR1>3.0.CO;2-S.

[2] G.Z. Yao, C.K. Mechefske, B.K. Rutt, Acoustic noise simulation and measurement of a gradient insert in a 4 T MRI, Appl. Acoust. 66 (2005) 957–973, https://doi.org/10.1016/j.apacoust.2004.11.006.

[3] N.B. Roozen, A.H. Koevoets, A.J. den Hamer, Active vibration control of gradient coils to reduce acoustic noise of MRI systems, IEEE/ASME Trans. Mechatr. 13 (2008) 325–334, https://doi.org/10.1109/TMECH.2008.924111.

[4] D. Le Bihan, C. Poupon, A. Amadon, F. Lethimonnier, Artifacts and pitfalls in diffusion MRI, J. Magn. Reson. Imag. 24 (2006) 478–488, https://doi.org/10.1002/jmri.20683.

[5] M. Markl, R. Bammer, M.T. Alley, C.J. Elkins, M.T. Draney, A. Barnett, M.E. Moseley, G.H. Glover, N.J. Pelc, Generalized reconstruction of phase contrast MRI: Analysis and correction of the effect of gradient field distortions, Magn. Reson. Med. 50 (2003) 791–801, https://doi.org/10.1002/mrm.10582.

[6] J. Van Vaals, A. Bergman, Optimization of eddy-current compensation, J. Magn. Reson. 90 (1990) 52–70, https://doi.org/10.1016/0022-2364(90)90365-G.

[7] D. Giese, M. Haeberlin, C. Barmet, K.P. Pruessmann, T. Schaeffter, S. Kozerke, Analysis and correction of background velocity offsets in phase-contrast flow measurements using magnetic field monitoring, Magn. Reson. Med. 67 (2012) 1294–1302, https://doi.org/10.1002/mrm.23111.

[8] J. Busch, S. Vannesjoe, D. Giese, C. Barmet, K.P. Pruessmann, S. Kozerke, Pre-emphasis compensation of oscillatory phase offsets in phase-contrast flow measurements, in: Int. Soc. Magn. Reson. Med., 2012, p. 1172.

[9] B.E. Dietrich, D.O. Brunner, B.J. Wilm, C. Barmet, S. Gross, L. Kasper, M. Haeberlin, T. Schmid, S.J. Vannesjo, K.P. Pruessmann, A field camera for MR sequence monitoring and system analysis, Magn. Reson. Med. 75 (2016) 1831–1840, https://doi.org/10.1002/mrm.25770.

[10] S.J. Vannesjo, M. Haeberlin, L. Kasper, M. Pavan, B.J. Wilm, C. Barmet, K.P. Pruessmann, Gradient system characterization by impulse response measurements with a dynamic field camera, Magn. Reson. Med. 69 (2013) 583–593, https://doi.org/10.1002/mrm.24263.

[11] S.J. Vannesjo, B.E. Dietrich, M. Pavan, D.O. Brunner, B.J. Wilm, C. Barmet, K.P. Pruessmann, Field camera measurements of gradient and shim impulse responses using frequency sweeps, Magn. Reson. Med. 72 (2014) 570–583, https://doi.org/10.1002/mrm.24934.

[12] S.A. Winkler, A. Alejski, T. Wade, C.A. McKenzie, B.K. Rutt, On the accurate analysis of vibroacoustics in head insert gradient coils, Magn. Reson. Med. 78 (2017) 1635–1645, https://doi.org/10.1002/mrm.26543.

[13] H. Sanchez Lopez, F. Freschi, A. Trakic, E. Smith, J. Herbert, M. Fuentes, S. Wilson, L. Liu, M. Repetto, S. Crozier, Multilayer integral method for simulation of eddy currents in thin volumes of arbitrary geometry produced by MRI gradient coils, Magn. Reson. Med. 71 (2014) 1912–1922, https://doi.org/10.1002/mrm.24819.

[14] E.K. Brodsky, A.A. Samsonov, W.F. Block, Characterizing and correcting gradient errors in non-cartesian imaging: Are gradient errors linear time-invariant (LTI)?, Magn Reson. Med. 62 (2009) 1466–1476, https://doi.org/10.1002/mrm.22100.

[15] M.A. Bernstein, K.F. King, X.J. Zhou, Handbook of MRI Pulse Sequences, Elsevier, 2004.

[16] Q. Liu, D.G. Hughes, P.S. Allen, Quantitative characterization of the eddy current fields in a 40-cm bore superconducting magnet, Magn. Reson. Med. 31 (1994) 73–76, https://doi.org/10.1002/mrm.1910310112.

[17] H.M. Gach, I.J. Lowe, D.P. Madio, A. Caprihan, S.A. Altobelli, D.O. Kuethe, E. Fukushima, A programmable pre-emphasis system, Magn. Reson. Med. 40 (1998) 427–431, https://doi.org/10.1002/mrm.1910400313.

[18] W.M. Spees, N. Buhl, P. Sun, J.J.H. Ackerman, J.J. Neil, J.R. Garbow, Quantification and compensation of eddy-current-induced magnetic-field gradients, J. Magn. Reson. 212 (2011) 116–123, https://doi.org/10.1016/j.jmr.2011.06.016.

[19] S. Robertson, D.G. Hughes, Q. Liu, P.S. Allen, Analysis of the temporal and spatial dependence of the eddy current fields in a 40-cm bore magnet, Magn. Reson. Med. 25 (1992) 158–166.

[20] J. Busch, S.J. Vannesjo, C. Barmet, K.P. Pruessmann, S. Kozerke, Analysis of temperature dependence of background phase errors in phase-contrast cardiovascular magnetic resonance, J. Cardiovasc. Magn. Reson. 16 (2014) 97, https://doi.org/10.1186/s12968-014-0097-6.

[21] A.M. El-Sharkawy, M. Schar, P.A. Bottomley, E. Atalar, Monitoring and correcting spatio-temporal variations of the MR scanner's static magnetic field, Magn. Reson. Mater. Phys. Biol. Med. 19 (2006) 223–236, https://doi.org/10.1007/s10334-006-0050-2.

[22] C. Boesch, R. Gruetter, E. Martin, Temporal and spatial analysis of fields generated by eddy currents in superconducting magnets: Optimization of corrections and quantitative characterization of magnet/gradient systems, Magn. Reson. Med. 20 (1991) 268–284, https://doi.org/10.1002/mrm.1910200209.

[23] A. Bhogal, M. Versluis, J. Koonen, J.C.W. Siero, V.O. Boer, D. Klomp, P.R. Luijten, H. Hoogduin, Image-based method to measure and characterize shim-induced eddy current fields, Conc. Magn. Reson. Part A. 42 (2013) 245–260, https://doi.org/10.1002/cmr.a.21290.

[24] M. Terpstra, P.M. Andersen, R. Gruetter, Localized eddy current compensation using quantitative field mapping, J. Magn. Reson. 131 (1998) 139–143, https://doi.org/10.1006/jmre.1997.1353.

[25] P. Jehenson, M. Westphal, N. Schuff, Analytical method for the compensation of eddy-current effects induced by pulsed magnetic field gradients in NMR systems, J. Magn. Reson. 90 (1990) 264–278, https://doi.org/10.1016/0022-2364(90)90133-T.

[26] F.J. Harris, On the use of windows for harmonic analysis with the discrete Fourier transform, Proc. IEEE. 66 (1978) 51–83, https://doi.org/10.1109/PROC.1978.10837.

[27] R.W. Brown, Y.N. Cheng, E.M. Haacke, Magnetic Resonance Imaging: Physical Principles and Sequence Design, John Wiley & Sons Ltd, Chichester, UK, 2014, https://doi.org/10.1002/9781118633953.

[28] M.a. Schofield, Y. Zhu, Fast phase unwrapping algorithm for interferometric applications, Opt. Lett. 28 (2003) 1194–1196, https://doi.org/10.1364/OL.28.001194.

[29] K.N. Magdoom, A. Zeinomar, R.R. Lonser, M. Sarntinoranont, T.H. Mareci, Phase contrast MRI of creeping flows using stimulated echo, J. Magn. Reson. 299 (2019) 49–58, https://doi.org/10.1016/J.JMR.2018.12.009.

[30] I. Swan, M. Reid, P.W.A. Howe, M.A. Connell, M. Nilsson, M.A. Moore, G.A. Morris, Sample convection in liquid-state NMR: why it is always with us, and what we can do about it, J. Magn. Reson. 252 (2015) 120–129, https://doi.org/10.1016/j.jmr.2014.12.006.

[31] C.B. Markwardt, Non-linear least squares fitting in IDL with MPFIT, in: Astronomical Society of the Pacific: San Francisco, Quebec, Canada, 2009, pp. 251–254.

[32] M. Longnecker, R. Ott, A first course in statistical methods, Thomas Brooks/Cole, Belmont, 2004.

[33] N.O. Addy, H.H. Wu, D.G. Nishimura, Simple method for MR gradient system characterization and k-space trajectory estimation, Magn. Reson. Med. 68 (2012) 120–129, https://doi.org/10.1002/mrm.23217.

[34] P.T. Callaghan, Translational Dynamics and Magnetic Resonance, Oxford University Press, 2011, https://doi.org/10.1093/acprof:oso/9780199556984.001.0001.

[35] N. Kickler, W. Van Der Zwaag, R. Mekle, T. Kober, J.P. Marques, G. Krueger, R. Gruetter, Eddy current effects on a clinical 7T–68 cm bore scanner, Magn.

Reson. Mater. Phys. Biol. Med. 23 (2010) 39–43, https://doi.org/10.1007/s10334-009-0192-0.

[36] A. Deshmane, V. Gulani, M.A. Griswold, N. Seiberlich, Parallel MR imaging, J. Magn. Reson. Imag. 36 (2012) 55–72, https://doi.org/10.1002/jmri.23639.

[37] C. Juchem, T.W. Nixon, S. McIntyre, V.O. Boer, D.L. Rothman, R.A. De Graaf, Dynamic multi-coil shimming of the human brain at 7 T, J. Magn. Reson. 212 (2011) 280–288, https://doi.org/10.1016/j.jmr.2011.07.005.

[38] C.T. Harris, W.B. Handler, B.A. Chronik, A new approach to shimming: The dynamically controlled adaptive current network, Magn. Reson. Med. 71 (2014) 859–869, https://doi.org/10.1002/mrm.24724.

[39] L.K. Tam, J.P. Stockmann, G. Galiana, R.T. Constable, Null space imaging: Nonlinear magnetic encoding fields designed complementary to receiver coil sensitivities for improved acceleration in parallel imaging, Magn. Reson. Med. 68 (2012) 1166–1175, https://doi.org/10.1002/mrm.24114.

[40] D. Gallichan, C.A. Cocosco, A. Dewdney, G. Schultz, A. Welz, J. Hennig, M. Zaitsev, Simultaneously driven linear and nonlinear spatial encoding fields in MRI, Magn. Reson. Med. 65 (2011) 702–714, https://doi.org/10.1002/mrm.22672.